Slip-rates along the Chaman fault: Implication for transient strain accumulation and strain partitioning along the western Indian plate margin

Shams Ul-Hadi [a,*], Shuhab D. Khan [b], Lewis A. Owen [c], Abdul S. Khan [d], Kathryn A. Hedrick [c], Marc W. Caffee [e]

[a] Berger Geosciences, 13100 Northwest Freeway, Houston, TX 77040, USA
[b] Department of Earth and Atmospheric Sciences, University of Houston, TX 77004, USA
[c] Department of Geology, University of Cincinnati, Cincinnati, OH 45221, USA
[d] Center of Excellence in Mineralogy, University of Baluchistan, Pakistan
[e] Department of Physics, Purdue University, West Lafayette, IN 47907, USA

ARTICLE INFO

ABSTRACT

The Chaman fault in Western Pakistan marks the western collision boundary between the Indian and Eurasian plates and connects the Makran subduction zone to the Himalayan convergence zone. Geomorphic-scale slip-rates along an active strand of the Chaman fault are added to the sporadic data set of this poorly investigated transform system. Field investigations coupled with high-resolution GeoEye-1 satellite data of an alluvial fan surface (Bostankaul alluvial fan) show ~1150 m left-lateral offset by the fault since the formation of the alluvial fan surface. A weighted mean ^{10}Be exposure age of 34.8 ± 3 kyr for the Bostankaul alluvial surface yields a slip-rate of 33.3 ± 3.0 mm/yr. This rate agrees with the geologically defined slip-rates along the Chaman fault, but is approximately twice as large as that inferred from the decade-long global positioning system measurements of 18 ± 1 mm/yr. The contrast in geomorphic and geodetic slip-rates along the Chaman fault, like other major intra-continental strike–slip faults, has two major implications: 1) the geodetic rates might represent a period of reduced displacement as compared to the averaged Late Pleistocene rate because of transient variations in rates of elastic strain accumulation; or 2) strain partitioning within the plate boundary zone. While strain partitioning could be the reason of slip-rate variations within the western Indian plate boundary zone, transient strain accumulation could explain contrasting slip-rates along the Chaman fault at this stage in its poorly understood seismic cycle.

© 2013 Elsevier B.V. All rights reserved.

1. Introduction

Models of the dynamics of large-scale intracontinental deformation are influenced by two end-member views: 1) highly localized deformation in which the lithosphere is deforming as a rigid plate (Avouac and Tapponnier, 1993; Meade, 2007; Peltzer and Saucier, 1996; Peltzer and Tapponnier, 1988; Tapponnier et al., 2001; Thatcher, 2007); and 2) regionally distributed, continuous deformation within the lithosphere which deforms in a fluid-like-fashion (Bendick et al., 2000; England and Houseman, 1986; Molnar and Tapponnier, 1975; Zhang et al., 2007). The Himalayan–Tibetan orogeny provides the opportunity to test these two hypotheses with advances in both GPS/InSAR techniques and in dating techniques to date Late Quaternary landforms and sediments, including, terrestrial cosmogenic nuclides (TCN) and ^{14}C methods. The plate bounding crustal scale strike–slip faults within the orogen are central to such studies. Rigid-plate localized deformation supports high long-term (10^3–10^6 years) geomorphic slip rates (Chevalier et al., 2005; Mériaux et al., 2004, 2005; Tapponnier et al.,

2001; Van der Woerd et al., 1998, 2000), while diffused deformation is supported by relatively low short-term (10^0–10^1 years) geodetic slip rates along these major strike–slip faults (Bendick et al., 2000; Chen et al., 2000; England and Molnar, 2005; Phillips et al., 2004; Shen et al., 2001).

Defining the temporal and spatial distribution of strain along plate boundaries is challenging, but is essential for developing and testing tectonic models. This is particularly true for the Himalayan–Tibetan orogen, which is one of the most logistically and politically difficult regions to study, yet ideal for examining the nature and dynamics of continent–continent collision. In brief, the Himalayan–Tibetan orogen formed from the collision of the Indian and Eurasian continental lithospheres (Yin and Harrison, 2000). Underthrusting of the Indian plate beneath the Himalaya accommodates around half (Thatcher, 2007) of its 36–45 mm/yr northward movement (Klootwijk et al., 1998; Molnar and Stock, 2009), but much of the remaining movement is adjusted within the Tibet plateau, either localized along the crustal scale strike–slip faults (Tapponnier et al., 2001) or distributed within the blocks bounded by these strike–slip faults (England and Molnar, 2005; Zubovich et al., 2010). While many studies (Bendick et al., 2000; Chevalier et al., 2005; He and Chéry, 2008; Wright et al., 2004) have focused on understanding the deformation along these mega-structures

* Corresponding author.
E-mail addresses: sulhadi@b-geo.com, shams_ogdc@yahoo.com (S. Ul-Hadi).
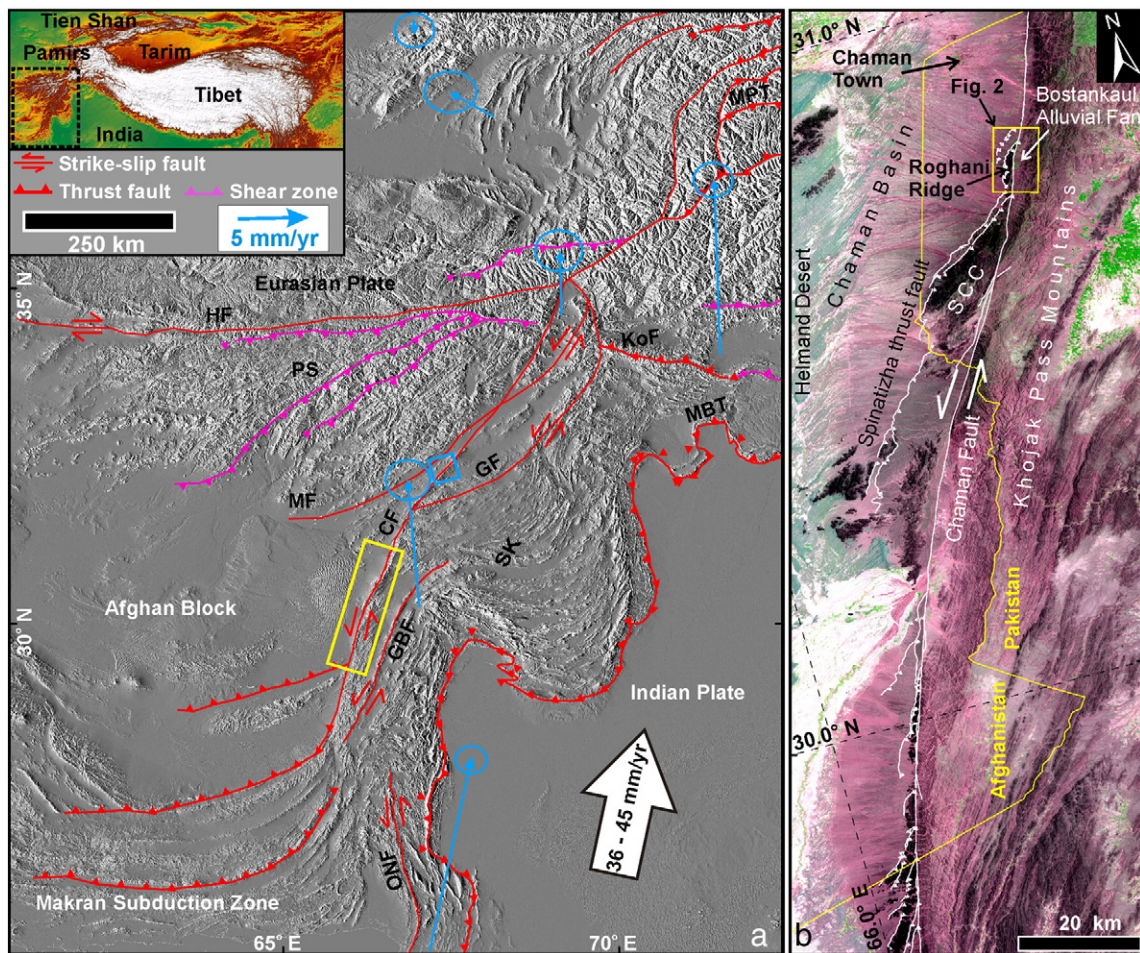
Fig. 1. (a) Tectonic framework of the northwestern Indian Plate margin and Eurasia. Major active strike–slip faults, thrusts and suture zones (modified after Mohadjer et al., 2010; Taylor and Yin, 2009) are displayed on SRTM elevation data. Blue arrows show GPS velocities with respect to fixed Eurasian plate/Afghan block (Mohadjer et al., 2010). The blue box is the position of Synthetic Aperture Radar (SAR) data used in InSAR studies (Furuya and Satyabala, 2008). Notice the azimuth of the Indian plate motion (N12°E) against the average N34°E azimuth of the strike of the CF is responsible for the strain partitioning in the Suliman–Kirthar Fold-thrust Belt (SK). The yellow rectangle shows position of part B. GF: Gardiz Fault; HF: Herat Fault; KoF: Konar Fault; MBT: Main Boundary Thrust; MF: Mokur Fault; MPT: Main Pamir Thrust; ONF: Ornach-Nal Fault; PS: Panjao shear. The inset map shows location of (a) within the Himalayan–Tibetan orogen. (b) Central section of the Chaman fault (CF) in western Pakistan shown on an Advanced Spaceborne Thermal Emission and Reflection Radiometer (ASTER) image (bands 1-3-2 displayed as RGB). The gentle bend in strike of the CF just north of the present study area helps create the Spinatizha thrust fault and the transpression uplifting the Spinatizha Crystalline Complex (SCC), and a part of the alluvial fan complex of the Chaman basin (Center of the map). Yellow box shows the location of the Bostankaul alluvial fan and Roghani Ridge in Fig. 2.

in the Himalaya and Tibet, little focus has been given to the western Indian plate boundary, which is largely defined by the Chaman transform fault system (Fig. 1a). It has been thought that the Chaman fault zone does not play any significant role in accommodating shortening between the Indian and Eurasian plates so it has been largely ignored, and adding to this is the civil unrest in this region, which hinders access to critical sites.

The geomorphic expression of the Chaman fault system is evident throughout its entire length of ~860 km along the border regions of Pakistan and Afghanistan. The shear zone is most apparent at the contact between the Quaternary alluvial deposits to the west and the meta-sediments of the Late Eocene to Oligocene Katawaz Basin (Carter et al., 2010) to the east of the fault (Ruleman et al., 2007; Fig. 1). The fault also brings slivers of the Late Jurassic to Cretaceous arc rocks west of the fault zone in contact with the meta-sediments in some places (Lawrence et al., 1981). The shear zone varies in width with linear zones of <1 km wide to about 20 km wide zones of multiple strands with conjugate Riedel shears and thrust fault systems (Lawrence and Yeats, 1979; Wheeler et al., 2005). The strike of the fault ranges from N10°E to N35°E (Lawrence et al., 1992) resulting in

several double bends responsible for the popup zones that are present throughout its length. Several incipient transpressional structures of varying sizes have been reported throughout the length of the fault system (Ruleman et al., 2007; Ul-Hadi et al., 2012). The difference in azimuth of the Indian plate movement and strike of the Chaman fault system essentially requires some convergence (Molnar and Dayem, 2010), which is accounted for by these features, and is a phenomenon that shapes the geomorphic expression of a strike–slip fault system (Frankel and Owen, 2013).

Recent GPS and InSAR studies on the Chaman fault yield slip rates of 18 ± 1 mm/yr (Mohadjer et al., 2010) and a post-seismic slip-rate of ~8 mm/yr (Furuya and Satyabala, 2008; Fig. 1a; Table 1). Lawrence et al. (1992) obtained a larger slip-rate over a geologically longer (>10⁶ years) timescale. They defined a displacement of 460 ± 10 km, which was based on: 1) the presence of a major thrust fault that is laterally displaced for ~250 km on both sides of the Chaman fault; 2) the correlation of subduction complexes present on both sides of the fault; 3) the depression of the Kharan desert south of the Ras Koh that is equivalent/correlated to that of the Ab-e-Istada depression south of the Gardez fault, and (4) the sediment of the eastern Makran Ranges

Table 1
A compilation of previously reported offsets and slip-rates along the Chaman fault.

Slip-rate (mm/yr)	Location	Methods/features used	Reference
08.0	31.96°N, 67.55°E	InSAR (a Mw 5.0 earthquake, Oct. 21, 2005)	Furuya and Satyabala (2008)
18 ± 1	Northern segment where Chaman fault bifurcates in to two strands	GPS observations over a seven years' time period	Mohadjer et al. (2010)
19–24	Central segment of the fault from 29° N to 35° N near Chaman	Matching four features displaced along the fault	Lawrence et al. (1992)
25–35	Northern segment of the fault in Afghanistan	~80 km displacement in a 2 Ma old volcanic unit and extrapolating the rate to the Chaman fault	Beun et al. (1979)

that is equivalent/correlated to the sediment of the Katawaz Basin. These offsets/correlations imply an average slip rate of 19–24 mm/yr since the inception of the strike–slip motion on the Chaman fault at 25–20 Ma (Lawrence et al., 1992). Beun et al. (1979) extrapolated an ~60–80 km offset along a north–south fault of a volcanic unit dated at ~2 Ma to the Chaman fault and estimated a slip-rate of 25–35 mm/yr. We present here the first [10]Be TCN surface exposure ages on a displaced alluvial fan—the Bostankaul alluvial fan (Fig. 1b)—along the Chaman fault to provide geomorphic rates of displacement and further insight on the evolution and recent strain accumulation along the western Indian plate boundary zone. We examine the differences between short-term geodetic slip rates and those based on longer timescale geomorphic and geologic observations to provide insights into the tectonic evolution of the Chaman fault and to aid in future seismic hazard assessment in the region.

2. Fault displacement and TCN ages

2.1. Tectonic setting of the site

The Bostankaul alluvial fan is located within the Chaman Basin near the village of Bostankaul (30.75°N/66.48°E at ~2000 m above sea level) and is morphostratigraphically among the oldest preserved alluvial fans displaced by the Chaman fault (Ul-Hadi et al., 2012; Fig. 2 and Supplementary Fig. 1). The Chaman Basin is a ~80 × 20 km arc-shaped asymmetrical alluvial basin fed by a moderate to highly-incised, discontinuous ephemeral stream network. The basin formed in response to the transpressional uplift of the block comprising the Roghani Ridge, the Spintizha Crystalline Complex and a part of the Khojak Pass Mountains to the east of the Chaman fault. This basin is the depositional site for sediments derived from the Khojak Pass Mountains, Roghani Ridge and Spintizha Crystalline Complex (Fig. 1b). The Khojak Pass Mountains comprise a part of the Tertiary Katawaz Basin, a remnant of the Neo-Tethys ocean basin, which existed prior to the collision of the Indian plate with the Afghan block and was mainly filled with Tertiary deltaic to submarine fan sediment and late-stage molasse (Carter et al., 2010; Qayyum et al., 1996). The Helmand desert flanks the western side of the Chaman Basin, while two unnamed basins define the northern and southern ends of the Chaman Basin. The southern half of the Chaman basin is delimited by a complex transpressional structure along the eastern boundary of the basin, which comprises the Chaman strike–slip and the second order Spinatizha thrust faults (Ul-Hadi et al., 2012; Fig. 1b). A pop-up zone is present within the transpressional structure and is composed of the Spinatizha Crystalline Complex (SCC), a sliver from a pre- to syn-collision Cretaceous Chaghai–Kandahar arc system that was present on the southeastern boundary of Eurasia (Lawrence et al., 1981, 1992), and an alluvial fan surface uplifted along the Spinatizha fault (Ul-Hadi et al., 2012).

2.2. Offset

Displacement along a strand of the Chaman fault in the study area was measured based on three geomorphic observations to help minimize the uncertainty associated with its determination (e.g. Chevalier et al., 2005; Cowgill et al., 2009; Frankel and Owen, 2013; Owen et al.,

2011). The landforms that helped in deciphering the total displacement are: (1) displaced alluvial fan sediment; (2) offset and deflected streams; and (3) presence of wind and water gaps reflecting left-lateral displacement. A concise account of these features is given below.

2.2.1. Bostankaul alluvial fan site

The displaced Bostankaul alluvial fan was mapped in the field and by using GeoEye-1 imagery. At this site the Bostankaul alluvial fan (surface/sediments mapped as Qf1) overlies the rocks of the Khojak Pass Mountains to the east and is terminated to the west by a faulted contact with a ridge called the Roghani ridge (the northern most extreme of the SCC; Figs. 1b and 2). The geomorphology of the Roghani ridge is described in more detail in Ul-Hadi et al. (2012). In the south, the Bostankaul alluvial fan has an erosional contact with a younger generation of alluvial fans (mapped as Qf3), while in the north, the main part of the Bostankaul alluvial fan coalesces with another displaced alluvial fan of approximately the same age to form a bajada. On the west side of the Chaman fault, where the Bostankaul alluvial fan borders the rocks of the Roghani Ridge, the Chaman fault traverses the main body of the alluvial fan and displaces it left-laterally. The southward-displaced part of the alluvial fan stands high up to ~15–30 m above the present depositional surface making the only east-facing fault scarp that is present within the study area (Fig. 2c). On average this part of the alluvial fan lies almost at the same topographic level (~1850 m above sea level) as the northward-displaced portion of the Bostankaul alluvial fan that lies east of the Chaman fault (Fig. 3). The alluvial surface has an average gradient of ~8 m/km from east to west and records stream avulsion and incision as up to ~40 m deep (Fig. 3a). On the southern periphery of the Bostankaul village there is a sharp slope discontinuity of about 30–35 m (Figs. 3a and 4b), while northern limit of the Bostankaul alluvial fan is not clearly defined because of the two coalescing alluvial fans that form a bajada (Fig. 2). This discontinuity in slope at the southern extreme of the alluvial fan surface marks the southern boundary of the Bostankaul alluvial fan and we use this discontinuity as a piercing point. Although this line of reference may have been reworked by erosional processes due to the presence of an active ephemeral stream, the alluvial sediment present on both sides of this line is distinctive from each other (Fig. 4a). This southern erosional termination of the Bostankaul alluvial fan east of the fault line is marked by a small patch of alluvial fan that is left over either from the main alluvial fan body or an eroded away younger alluvial fan surface.

The sediment of the Bostankaul alluvial fan (Qf1) is marked by soil development and lithification to a level, which is lacking in sediment piles (Qf3) present south of the Bostankaul alluvial fan (Qf1) (Fig. 4). Non-cohesive to granular soil is developed in the Qf1 surface to a depth of ~1 m (Ul-Hadi et al., 2012). Rock fragments of gravel and sand sizes make the bulk of this soil horizon. In highly leached zones these soils are more cohesive. Most of the human settlements (villages and fields) are inhabited on these surfaces where water is available (Figs. 2 and 4). Fanglomerates are not exposed commonly within the Qf1 surface, but can be seen mostly along the stream banks or in thrust blocks west of the Chaman fault. Qf3 surfaces are more uniform and unconsolidated having little stream incision, and mostly undeformed (Figs. 2c and 4c). The southward displaced part of the Bostankaul alluvial fan is an outlier comprising sediment correlating to the main alluvial
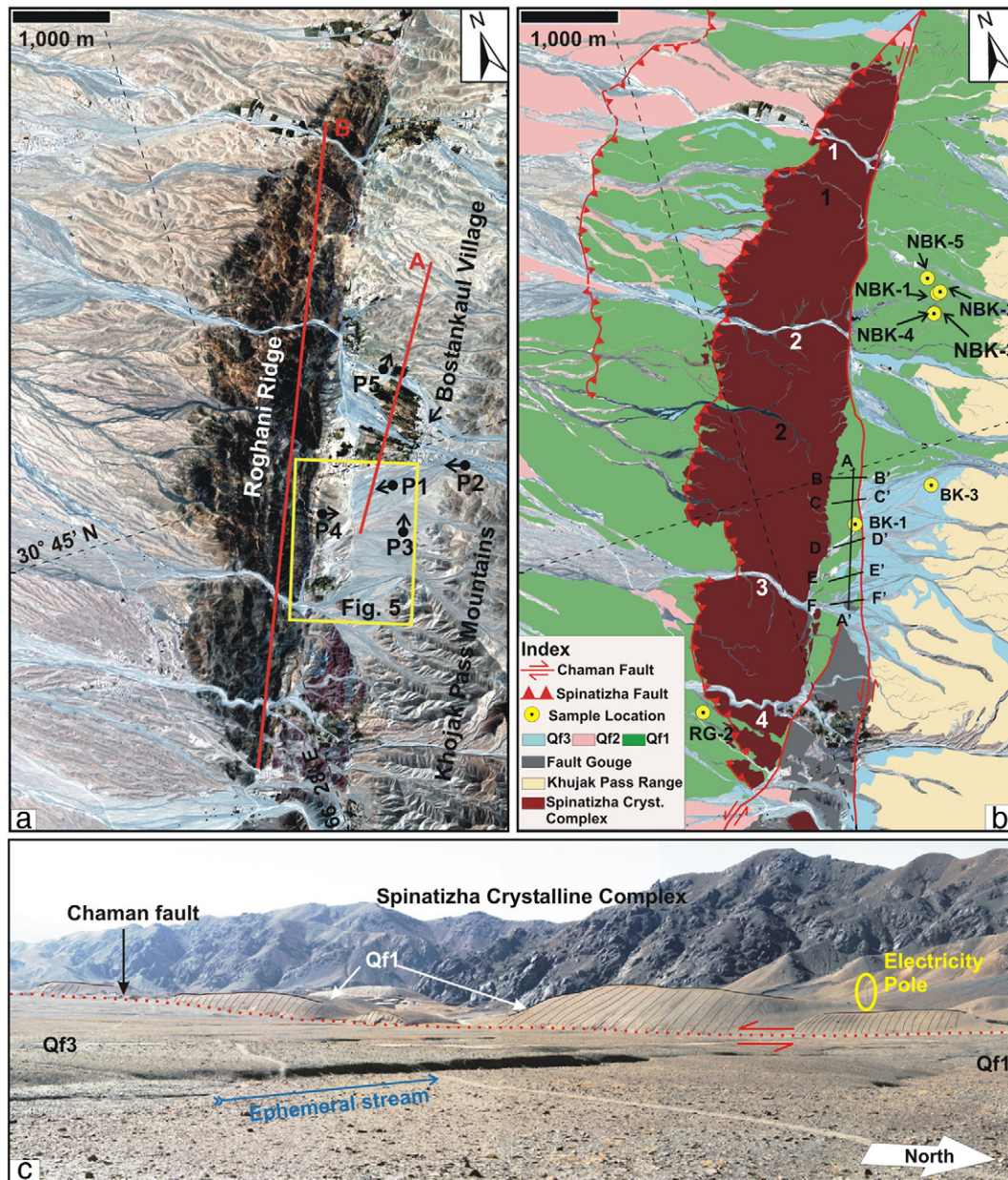
Fig. 2. Geology and geomorphology around the Roghani ridge and Bostankaul alluvial fan. (a) GeoEye-1 satellite image (Red-Green-Blue) of the Bostankaul alluvial fan and Roghani ridge. The stream (narrow whitish feature cutting in center across the ridge) that contributed to the alluvial fan surface is represented by east–west directed paleo-channel also cutting across the ridge although at a higher altitude (dark grayish linear feature south of the main stream). Yellow box shows location of the Fig. 4c. The red lines A and B are the transect lines for the profiles shown in Figs. 3a and 6b, respectively. The bullet-tailed arrows with numbered letter P show capture location and look direction of the field photographs shown in Figs. 2c and 4a–d. (b) Alluvial fan surfaces Qf1 to Qf3 and bedrock superimposed on a GeoEye-1 image with the locations of dated samples. The ridge is dissected by four water gaps (white numbers 1 to 4) and two wind gaps (black numbers 1 to 2) corresponding to the northern (1) and central (2) water gaps. The positions of these wind and water gaps record left-lateral movement along the Chaman fault at different time scales. Black lines AA′ to FF′ are the profile lines in Fig. 5b. (c) Field photograph showing a part of the Bostankaul alluvial fan (Qf1), a younger alluvial fan (Qf3) just south of the BF, and Roghani ridge, as been relocated by a strand of the Chaman fault. West-southwest looking view of a part of BF that lies to the west of the Chaman fault and which is displaced towards south from the main BF body in the north. This part of the fan is making an east facing fault scarp with a maximum vertical height of ~40 m where sample # BK-1 was collected from a meter-sized sandstone boulder. Notice the smooth comparatively less incised surface of the Qf-3. An ephemeral stream to the north of the Qf-3 surface separates it from the Qf-1 surface.

fan sediment based on its top soil horizon, relatively good lithification, and deep erosion (Figs. 2c and 4). There are about four small mounds lined along a straight north–south line marking an east facing fault scarp (Figs. 2 and 4). The southernmost sediment pile is the last preserved patch of the Bostankaul alluvial fan; we use this as the second piercing point to measure the total displacement along the Chaman fault (Fig. 5).

2.2.2. Stream deflections

Stream abandonment and deflection are common along most of the length of the Chaman fault and is more evident at the contact of the alluvial deposits and the bedrock (Lawrence et al., 1992; Ul-Hadi et al., 2012). Drainage patterns along active strike–slip faults are a time-dependent complex phenomenon and can lead to over estimation of the fault movement (Frankel and Owen, 2013). We used beheaded and deflected streams to calculate the left-lateral displacement along the Chaman fault in the study area. Transverse stream networks (s1 to s3) progressively cut across the shutter ridge that has developed at the downstream side of the fault (Fig. 5a). Initially the shutter ridge captured the stream (t1) resulting in deflection (t2) and ultimate abandonment (t2 through t4). The abandoned downstream part of the channel (s1) was reoccupied by another stream (s2), which was captured by the
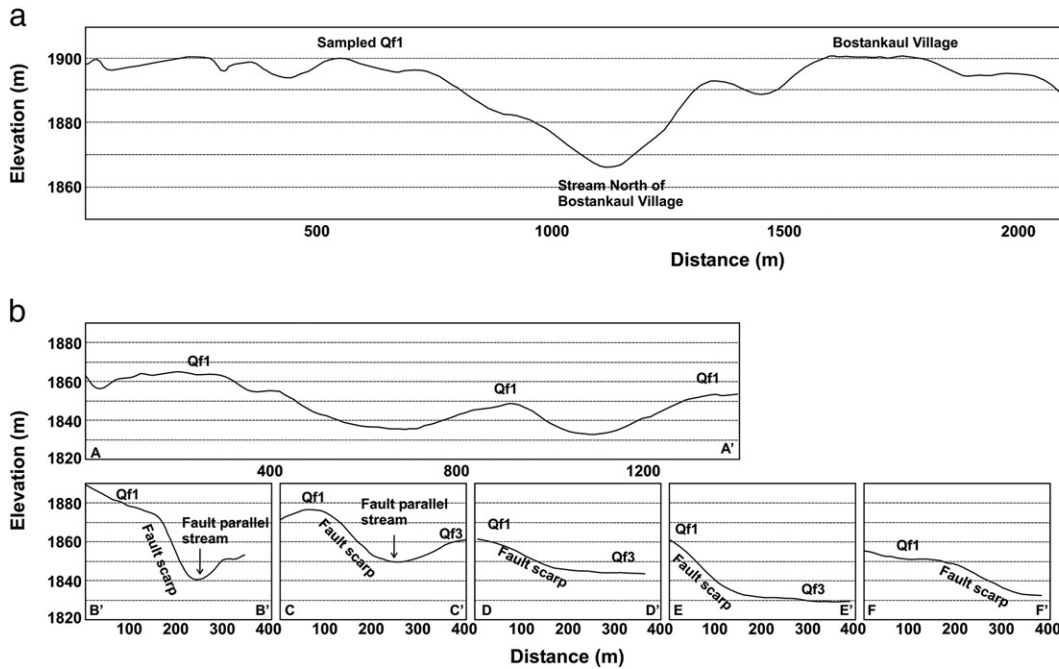
Fig. 3. (a) Surface expression of the northward-displaced part of the Bostankaul alluvial fan (Qf1) and its association with Qf3 which lies almost ~40 m below the average Qf1 surface at ~1900 m above sea level. Bostankaul village which is located on a part of the Qf1 surface is separated from the main fan body by a major stream dissecting the alluvial surface. Notice the narrow V-shaped stream in the center of the profile depicting fast incision and uplift. For location of the profile lines see Fig. 3a. (b) Surface expression and geometry of the fault scarp along the southward displaced part of the Bostankaul alluvial fan west of the Chaman fault. Longitudinal surface profile of this Qf1 body (AA′) shows three small yet prominent sediment bodies separated by two ephemeral streams. This incised body of alluvial sediment was once a continuous block displaced intact along the fault making a shutter ridge and has caused stream capture and ultimate abandonment. Surface profiles orthogonal to the fault trace showing the east facing fault scarp (BB′–FF′). This Qf1 body makes a sharp east facing fault scarp which rises ~15 m in the south to more than 30 m in the north above the Qf3 surface The almost vertical fault scarp is a continuous plane of more than 1000 m length from the Bostankaul village in the north to the southern limit of the Qf1. For location of the profile lines see Fig. 3b.

fault movement and is present to the left of the stream s1. While the first stream (s1), which has been captured and abandoned by the shutter ridge and fault movement cut across the ridge as s0 in order to keep its course. The phenomenon is repeated several times with the continued activity along the fault resulting in several beheaded streams (t3 and t4) cutting across the shutter ridge. Restoration of the original stream to the beheaded streams can help in estimating the final displacement along a fault.

The southward displaced part of the Bostankaul alluvial fan, which is present to the west of the Chaman fault, has acted as a shutter ridge in shaping the stream network of the area. This east facing fault scarp bounded ridge is comprised of four small patches of alluvial fan sediments (Figs. 2 and 5). These sediment patches were once a continuous unit displaced as a single block but are now incised by three beheaded ephemeral streams that have flowed across the ridge from east to west (Fig. 5b). The continued left-lateral movement of the Chaman fault has caused simultaneous stream capturing, deflection, abandonment, and ultimate incision of this pile of alluvial sediment, as been explained in Fig. 5a, in a way that has resulted in the present day geomorphology of the area (Fig. 5b).

2.2.3. Roghani ridge

This 8 × 1.5 km lenticular shaped ridge (Fig. 2) is the northern extremity of the transpression comprising rocks of the Spinatizha Crystalline Complex. This is an isolated ridge that has recorded simultaneous progressive uplift associated with the northward propagation of the Spinatizha thrust and left lateral displacement along the Chaman fault (Ul-Hadi et al., 2012). The continued movement along the Chaman fault system formed four prominent transverse water gaps and two corresponding wind gaps that traverse the ridge (Fig. 2). The development of wind and water gaps, is common along growing structures especially

along the thrust bounded folds (Burbank et al., 1996; Keller and DeVecchio, 2013). It is essential to have at least two sets of wind and water gaps in a growing fault-bounded fold to estimate any lateral growth and direction of an active fault system (Azor et al., 2002). In the case of Roghani ridge we have observed two prominent water gaps with their corresponding wind gaps arranged in a way that supports northward growth of the Spinatizha thrust and left-lateral movement along the Chaman fault (Fig. 6). The abandoned stream, which we assume as the past course of the present ephemeral stream (central water gap at ~1800 m above sea level) that cut across the center of the Roghani ridge may have fed to the Bostankaul alluvial fan is 77 ± 15 m above the water gap. Laterally the two gaps are 1348 ± 15 m apart with the water gap to the north of the wind gap implying a left lateral displacement and northward propagation of the ridge (Fig. 6). The other set of wind and water gaps at the northern end of the ridge also reinforce same sense of motion but with smaller lateral displacement (~450 m) and vertical uplift (~56 m) recording a younger activity along the Chaman fault system. The water gaps in the southern end of the ridge pose a complex evolution history with no preserved wind gap and will complicate further restoration of the displacement recorded by Bostankaul alluvial fan.

### 2.2.4. Observed displacement

The southward-displaced part of the Bostankaul alluvial fan was restored to its original position utilizing morphostratigraphy of the alluvial fan surfaces (Qf1–Qf3) and the ephemeral stream network of the area. Restoring the Qf1 surface back to its most probable original position, considering the geometry of the main stream that has fed to the alluvial surface and the abandoned streams that cut across the southward-displaced part of the main alluvial surface, shows a total displacement of 1150 ± 55 m (Fig. 5d–f). The average stream width of about 35–
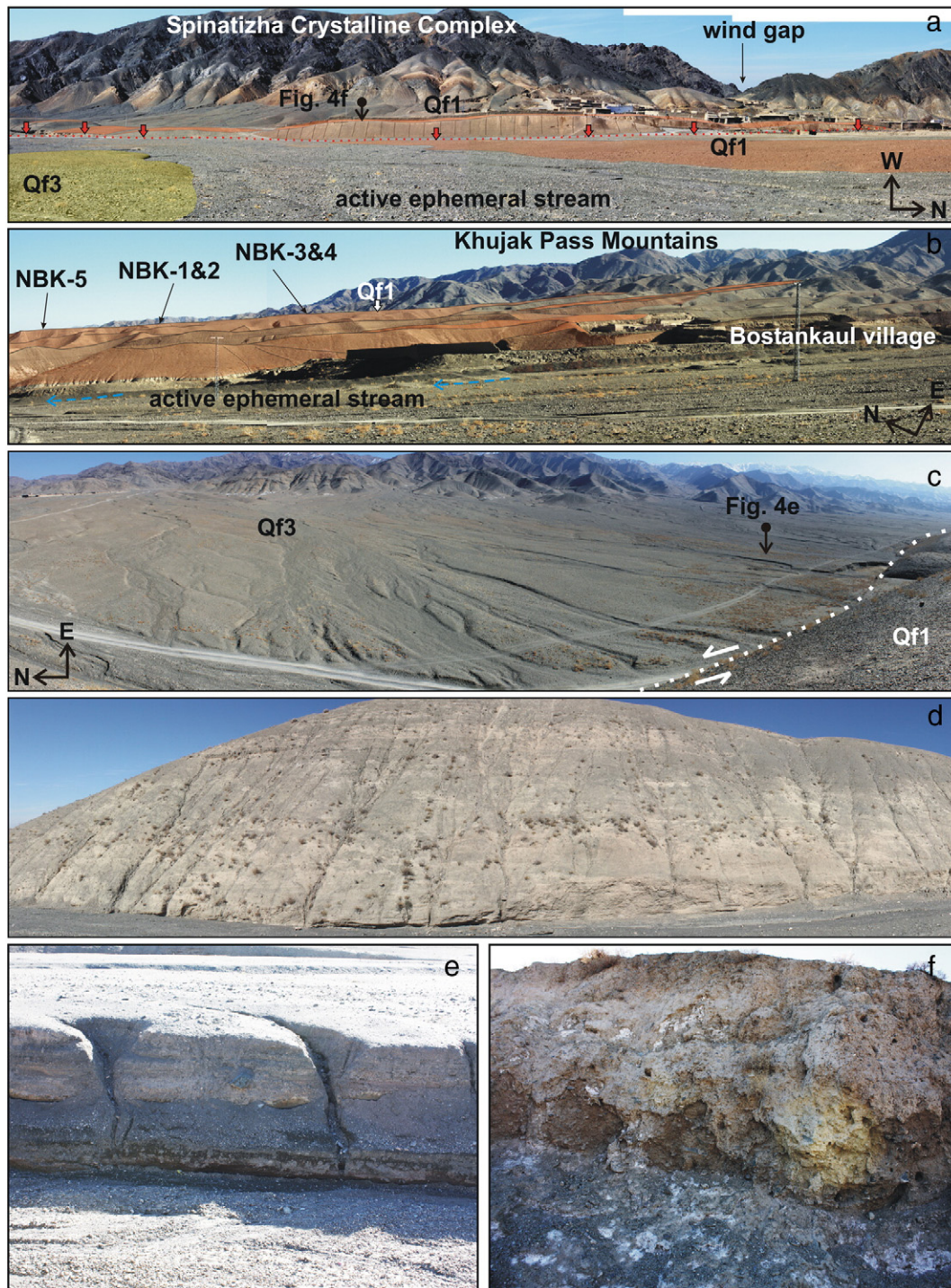
Fig. 4. (a) View of the ephemeral stream that separates Qf-1 and Qf-3 surfaces and flowing orthogonal to the displaced part of the Qf-1 where it diverts towards south and follow a course longitudinal to the Spinatizha crystalline complex. Red arrows point to the trace of the fault. (b) Main surface of the Bostankaul alluvial fan where most of the samples are collected. The overall surface is flat with a westward gradient of ~8 mm/m. Narrow streams with vertical and well-defined banks have incised the surface which is contrary to the Qf-3 surface (see Fig. 2c). The five samples that were collected from this surface are well spaced and settled in central parts of the flat surfaces with almost no burial or erosional signatures. (c) Field view of a Qf3 surface with little or no incision. These generations of the alluvial surfaces are smooth and flat lying showing less deformation as compared to the Qf1 surfaces. (d) An about 40 m vertical section within a Qf1 surface incised by a stream showing a well-lithified succession. (e) A close-up view of a vertical section in a Qf3 surface exposed in a stream. Qf3 sediments are unlithified and devoid of any soil development. (f) Field view of an upper section of a Qf1 surface showing extreme leaching and soil formation. All Qf1 surfaces are marked by soil development supporting human settlements where water is present as in Bostankaul village which resides on a Qf1 surface.

40 m (Ul-Hadi et al., 2012) adds to the total uncertainty in measuring displacement recorded by this displaced part of the alluvial fan body, to the otherwise sharp lines of reference i.e. the southern erosional boundary of the main alluvial fan east of the fault and the southern-most patch of Qf1 sediment west of the fault. Entrenchment of the shutter ridges and development of the transverse drainage along the growing structures is a complex phenomenon (Burbank et al., 1996; Keller and DeVecchio, 2013; Pearce et al., 2004) and can add significant
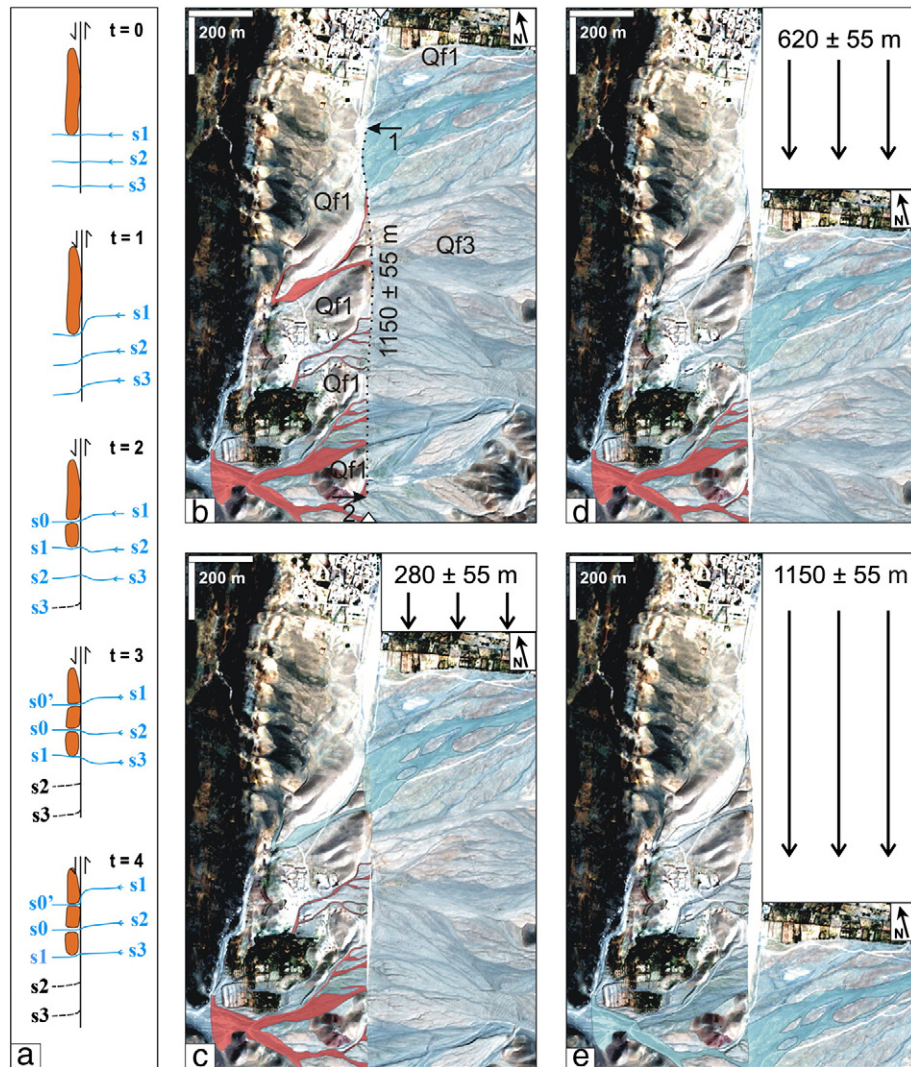
Fig. 5. Schematic representations and geomorphological interpretations of the displaced landforms and transverse streams pattern across a shutter ridge along an active strand of the left-lateral Chaman fault. (a) Progressive representation of stream deflection and ultimate abandonment through time due to left-lateral movement observed along the Chaman fault in area where the shutter ridges develop on the western side of the fault. Initially the streams flowing orthogonal to the fault get deflected (during t = 1) and eventually abandoned (dotted lines). The upstream portion of the stream cut across the ridge forming a new channel (s0) (during t = 2) while the abandoned downstream part (s1) is reactivated as the downstream portion of streams to the south (s2). With continued left-lateral movement the process repeats several times (e.g. during t = 3 and t = 4). (b) Present day stream network flowing across the Chaman fault in the Bostankaul alluvial fan area. The active stream (blue) is captured along the fault trace. Abandoned downstream portions of this stream are shown in red. Left lateral offset along the Chaman fault is recorded by the southward displaced part of the Bostankaul alluvial fan forming an east facing fault scarp and abandoned streams. Dotted black line shows the measured displacement of 1150 ± 55 m along this segment of the fault between the two pinning points 1 and 2 at the interface of the Qf1 and Qf3 alluvial fan sediment. Arrow heads at the top and bottom of the image show the trace of the fault. (c), (d), and (e) Restoration of the active stream to its three downstream beheaded channels that cut-across the shutter ridge. The final restoration accounts for 1150 ± 55 m total displacement.

uncertainty to the apparent displacement along the faults (Frankel and Owen, 2013). However, in the study area the presence of Qf1 sediments on both sides of the Chaman fault allows restoration of the displaced alluvial sediment to its most possible original geometry. Although the timing of the entrenchment of Qf1 west of the fault is unknown the four mounds which are composed of Qf1 sediment were once a single body of sediment that was displaced southward along the fault. This is supported by the similarity in sediment type within each individual mound, the presence of these sediments at the same topographic level, their soil development, and the landform with an eastward facing fault scarp. A stepwise restoration of the Qf1 surface west of the Chaman fault using the beheaded streams that cut across this sediment body gives ~280 m displacement (Fig. 5c) in case of the northernmost stream, ~620 m (Fig. 5d) in case of the central stream, and finally ~1150 m displacement (Fig. 5e) in case of the southernmost stream (Fig. 2b). The

timing and mechanism of entrenchment are explained in Fig. 5a with t = 4 representing the present day landscape. The final displacement of ~1150 m is further supported by the topography of the Roghani ridge with the present positions of the adjacent water and wind gaps in center of the ridge, which are laterally separated by ~1350 m showing a left-lateral sense of movement.

2.3. [10]Be TCN dating

Eight samples were collected for [10]Be TCN dating from the three different alluvial fan surfaces, including six from the Bostankaul alluvial fan surface (Qf1), which records the total displacement of 1150 ± 55 m (Table 2; Fig. 2). The samples were collected from well-embedded sandstone boulders, typically meter-sized, that have well developed rock varnish and were sourced from the Khojak Pass Mountains (Fig. 7a
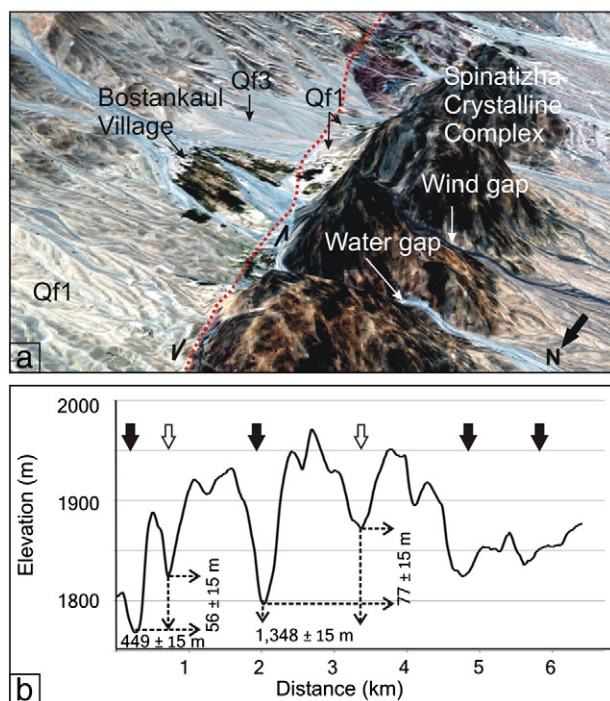
Fig. 6. (a) Perspective view extracted from GeoEye-1 data draped over ASTER DEM of the Roghani ridge, Bostankaul alluvial fan (Qf1 surface and Bostankaul village) and Qf3. The southward displaced part of the BF present west of the fault line (red dotted line) stands above the low lying Qf3. The older fan surface is deeply incised compared to the younger smooth surface. Roghani ridge is dissected by water gaps and wind gaps. (b) Longitudinal profile across the Roghani ridge. Note the gradual decrease in wind gaps (hollow arrows) and water gaps' (filled arrows) elevation towards north. The wind gap associated with the central water gap is been translated towards south 1348 ± 15 m, which reconciles with the surface dislocation of about ~1150 ± 55 m of the Bostankaul alluvial fan by a strand of the Chaman fault. The elevation difference of 77 ± 15 m between the two gaps accounts for the vertical uplift of the ridge. The northern set of wind and water gaps represent younger and continued activity of the Chaman strike–slip and Spinatizha thrust faults with ~450 lateral and ~55 m vertical displacements. Location of the profile line is marked in Fig. 2a.

and b). Boulders rich in quartz, with little evidence of weathering, were preferentially sampled. About 700–1000 g of sample was collected from the top 1–3 cm of each desired boulder using a hammer and chisel. The samples were crushed in the geochronology laboratories at the University of Cincinnati and quartz was separated from the 250–500 μm particle size fraction using the acid dissolution and heavy liquid separation as described in Owen et al. (2006, 2011). A low background Be carrier ($^{10}Be/^9Be < 8 \times 10^{-15}$) was added to the purified quartz and Be was separated using ion exchange chromatography. Be(OH)$_2$ was precipitated at pH > 7 and oxidized in quartz crucibles at a temperature of 700 °C. BeO was then mixed with Nb metal prior to determination of the $^{10}Be/^9Be$ ratio by accelerator mass spectrometry at the Purdue Rare Isotope Measurement (PRIME) Laboratory at Purdue University. SPEX beryllium standard (trace ICP/ICP-MS grade) at 1000 mg mL^{-1} in 2% HNO$_3$ was used for all samples and blanks. Two chemical blanks were processed and had a weighted mean $^{10}Be/^9Be$ ratio of 7.68 ± 2.24 × 10^{-15}. The Purdue Rare Isotope Measurement (PRIME) Laboratory accelerator mass spectrometer was calibrated using standard 200500020 from KN Standard Be 0152 with a $^{10}Be/^9Be$ ratio of 9465 × 10^{-15}. All $^{10}Be/^9Be$ ratios were converted to the revised ICN of Nishiizumi et al. (2007), which is the most commonly used AMS standard. Normalizing the measured isotopic ratios to this standard result in a production rate of 4.5 ± 0.3 ^{10}Be atoms/yr and a half-life of 1.36 Myr for age calculation (PRIME Laboratory). ^{10}Be concentrations in quartz were calculated from $^{10}Be/^9Be$ measured ratios using the

Table 2
Sample locations, descriptions, and summarized ^{10}Be TCN data and ages for three alluvial fan surfaces including the displaced Bostankaul alluvial fan.

Sample number	Surface	Lithology	Location Latitude	Longitude	Altitude	Size a/b/c axes	Thickness	Depth	Production rate (atoms/g/yr) Spallation[i]	Muons[j]	Shielding factor	Denudation rate	Quartz[a]	Be carrier	$^{10}Be/^9Be$[b,c]	^{10}Be concentration[d,e]	Age[f,g]	Age[f,h]
			°N	°E	(m asl)	(cm)	(cm)	(cm)				(mm/yr)	g	(mg)	×10^{13}	10^4 atoms/g SiO$_2$	kyr	kyr
NBK-1	Qf1	Sandstone	30.763	66.488	1926	90/50/40	1.5	0	14.86	0.335	1.0	0	21.585	0.3626	4.21 ± 0.17	64.12 ± 2.62	38.5 ± 1.6	38.5 ± 3.7
NBK-2	Qf1	Sandstone	30.763	66.488	1923	90/60/40	2	0	14.77	0.334	1.0	0	27.2966	0.3547	4.85 ± 0.18	57.14 ± 2.15	34.5 ± 1.3	34.5 ± 3.3
NBK-3	Qf1	Sandstone	30.761	66.488	1921	170/140/60	1	0	14.87	0.336	1.0	0	26.3834	0.3620	1.77 ± 0.17	22.04 ± 2.14	13.1 ± 1.3	13.1 ± 1.7
NBK-4	Qf1	Sandstone	30.761	66.488	1921	120/110/100	2.5	0	14.69	0.334	1.0	0	16.6977	0.3549	2.74 ± 0.14	52.82 ± 2.74	32.0 ± 1.7	32.0 ± 3.3
NBK-5	Qf1	Sandstone	30.765	66.488	1909	230/90/60	2.5	0	14.58	0.332	1.0	0	25.8119	0.3539	4.26 ± 0.16	52.96 ± 2.02	32.4 ± 1.3	32.4 ± 3.1
BK-1	Qf1	Sandstone	30.745	66.475	1884	130/50/40	2	0	14.39	0.330	1.0	0	14.9789	0.3462	2.97 ± 0.11	62.26 ± 2.35	38.6 ± 1.5	38.6 ± 3.7
BK-3	Qf3	Sandstone	30.747	66.482	1928	110/40/50	2	0	14.81	0.335	1.0	0	13.8512	0.3629	0.45 ± 0.06	10.76 ± 1.51	6.5 ± 0.9	6.7 ± 1.1
RG-2	Qf2	Sandstone	30.733	66.456	1826	130/90/80	1.5	0	13.91	0.325	1.0	0	11.5341	0.3451	1.16 ± 0.08	31.42 ± 2.13	20.1 ± 1.4	20.1 ± 2.2

[a] A density of 2.6 g cm^{-3} was used for all surface samples.
[b] Isotope ratios were normalized to ^{10}Be standards prepared by Nishiizumi et al. (2007) with a value of 2.85 × 10^{-12} and using a ^{10}Be half-life of 1.36 × 10^6 years.
[c] Uncertainties are reported at the 1σ confidence level.
[d] Samples were corrected for a mean blank $^{10}Be/^9Be = -7.68 \pm 2.24 \times 10^{-15}$.
[e] Propagated uncertainties include error in the blank, carrier mass (1%), and counting statistics.
[f] Beryllium-10 model ages were calculated with the CRONUS-Earth online calculator, version 2.2 (Balco et al., 2008; http://hess.ess.washington.edu/).
[g] Analytical uncertainty is quoted.
[h] Uncertainty quoted by propagated error in the model ages includes a 6% uncertainty in the production rate of ^{10}Be and a 4% uncertainty in the ^{10}Be decay constant.
[i] Constant (time-invariant) local production rate based on Lal (1991) and Stone (2000). A sea level, high-latitude value of 4.5 ± 0.3 at ^{10}Be g^{-1} quartz was used.
[j] Constant (time-invariant) local production rate based on Heisinger et al. (2002).
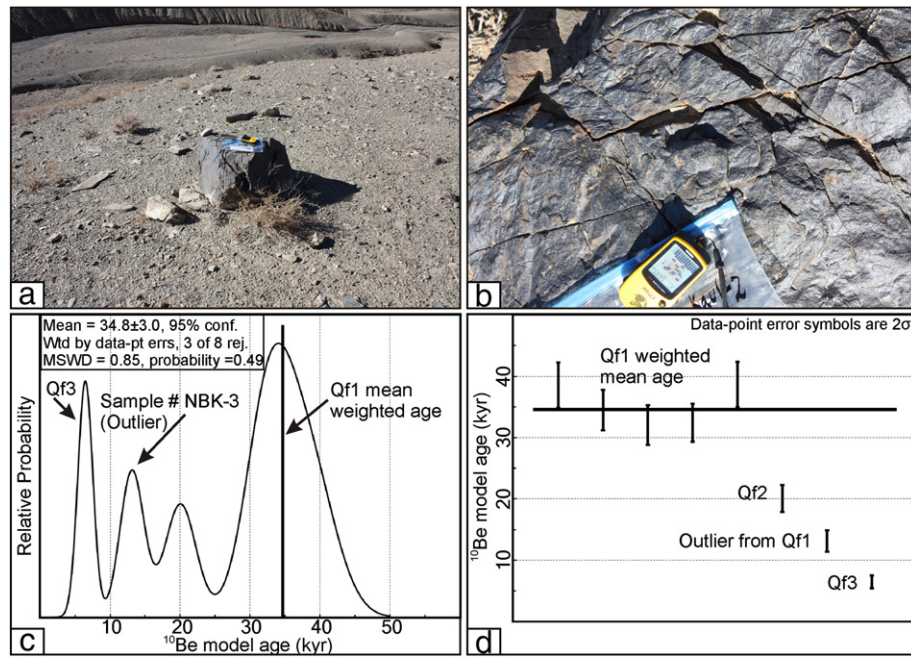
Fig. 7. (a) View of a typical boulder sample used in dating the BF surface. The meter-sized and well-set boulders on the flat surfaces showing no toppling or burial were sampled. All the samples collected from BF surface are well exposed having no apparent shielding of the cosmic rays. (b) A close-up view of the boulder in (a) showing complete desert varnishing and having no weathering effects of peeling off. (c) Probability density function (PDF) and (d) weighted mean of the [10]Be model ages of the Bostankaul alluvial fan. All the ages used in calculating the slip-rate cluster around weighted mean alluvial fan age of 34.8 ± 3.0 kyr excluding the outlier (Sample # NBK-3).

total Be in the samples and the sample weights. Production rates were scaled to the latitude and elevation of the Chaman sampling sites using the star scaling factors of Stone (2000) and an assumed 2.2% sea-level-high-latitude (SLHL) production muon contribution using the CRONUS-Earth online calculator version 2.2 (Balco et al., 2008; http://hess.ess.washington.edu/). These scaling factors reproduce the star scaling factors of Lal (1991). [10]Be concentrations were then converted to zero-erosion exposure ages using a SLHL [10]Be production rate of 4.5 ± 0.3 atoms/g quartz/yr (cf. Kubik and Ivy-Ochs, 2004; Nishiizumi et al., 1989). The impacts of topographic and depth corrections were determined by numeric integration of the flux corrected for the dip and topography at all azimuth directions (Nishiizumi et al., 1989).

TCN ages were calculated by applying the Stone (2000) and Lal (1991) time-independent model using the CRONUS-Earth online calculator, version 2.2 (Balco et al., 2008; http://hess.ess.washington.edu/). We use the time-independent model because of the continued debate regarding appropriate corrections and models for temporal variation in Earth's magnetic field. However, we recognize that different models may give up to 9–11% difference in ages. Slip rate studies generally use 4–10 [10]Be ages per surface to identify clustering and to help assess if there are the problems associated with erosion and/or exhumation of boulders that would result in underestimates of the true age of the surface or inheritance resulting in overestimates of the true age of the surface (Blisniuk et al., 2010; Chevalier et al., 2005; Frankel et al., 2007a,b).

2.3.1. [10]Be model ages

Our [10]Be ages, excluding the one outlier (Sample # NBK-3), are well clustered and tightly define the age of the displaced Bostankaul alluvial fan between 32 and 39 kyr (weighted mean age 34.8 ± 3.0 kyr (2σ error) excluding the outlier; Fig. 7c and d). The [10]Be age of 13.1 ± 1.7 kyr for sample NBK-3 is likely the result of enhanced weathering and/or toppling of the sampled boulder. The [10]Be age for a sample on southward-displaced part of the Bostankaul

alluvial fan is 38.6 ± 3.7 kyr (BK-1), which falls within the [10]Be age cluster for the main alluvial fan (Fig. 7).

The young age of 6.5 ± 1.1 kyr for sample BK-3, a boulder on an alluvial fan surface south of the displaced Bostankaul alluvial fan (Qf1), can be explained either as a boulder from within a much younger alluvial surface that formed after the abandonment of the Bostankaul alluvial fan—hence marking the southern fringe of the alluvial fan. Or the BK-3 sample by itself represents the southern extreme of the Bostankaul alluvial fan (Qf1) that has been uplifted and eroded away since the abandonment of Qf1 surface, resulting in a younger depositional age. The first possibility places an upper limit on the displacement to be 1150 ± 55 m, which is in agreement with the displacement recorded by the positions of the water and wind gaps. In contrast, restoration of the alluvial fan based on the eroded portion of the alluvial fan, from its presumed apex, yields a total displacement of about 880 ± 55 m for the Bostankaul alluvial fan surface.

The only dated sample west of the Roghani ridge dates to 20.1 ± 2.2 kyr, which we group with the ages of Bostankaul alluvial fan because of the sedimentological similarity in the two alluvial surface. The difference in the ages may reflect a more eroded alluvial surface west of the ridge in contrast to the alluvial surface present east of the Roghani ridge. Therefore the alluvial surface that we dated west of the ridge can be argued to be of the same generation of alluvial fan as the Bostankaul fan. This implies that the Bostankaul alluvial fan and alluvial fans west of the Roghani ridge pre-date the uplift of the ridge, which rises 77 ± 15 m above alluvial fan surface (Fig. 7), along the Spinatizha thrust fault.

3. Slip-rates

Matching the 1150 ± 55 m offset with the surface abandonment sample ages for the Bostankaul alluvial fan yields a geomorphic left-lateral slip rate ranging from 30.1 ± 2.9 to 36.2 ± 3.1 mm/yr, with an average of 33.1 ± 3.2 mm/yr. These geomorphic rates are consistent with the geologically (10[6] years) estimated slip-rates of

25–35 mm/yr and 19–24 mm/yr (Beun et al., 1979; Lawrence et al., 1992), although they are at the high range. In contrast, the geomorphic rates are more than two to four times that of the geodetically estimated rate of 18 ± 1 mm/yr (Mohadjer et al., 2010) and the post-seismic slip-rate of ~8 mm/yr that was estimated from InSAR analysis (Furuya and Satyabala, 2008).

4. Discussion

Multiple slip-rates are important for understanding the nature and development of fault systems (Frankel and Owen, 2013; Frankel et al., 2011). However, discrepancies between slip rates determined for different time intervals has led to contrasting interpretations including secular variations in slip-rate along faults (e.g. Chevalier et al., 2005; Frankel and Owen, 2013), and strain trade-off among interacting faults and fault inversion (e.g. Blisniuk et al., 2010; Hoeft and Frankel, 2010; Oskin et al., 2007). Some studies have tried to reconcile geodetic and geomorphic slip-rates (Cowgill et al., 2009).

The geomorphic slip-rate of 33.3 ± 3.0 mm/yr along a strand of the Chaman fault measured during this study is about double that of the geodetically estimated rate of 18 ± 1 mm/yr (Mohadjer et al., 2010) but in close agreement with the long-term slip-rates of 25–35 mm/yr and 19–24 mm/yr (Beun et al., 1979; Lawrence et al., 1992). The discrepancy between geomorphic and geodetic slip-rates in this area could be a result of either: 1) The mid-crust is fairly low viscosity in this area as indicated by the presence of ~20–25 km thick crystalline crust under the Chaman fault (Jadoon and Khurshid, 1996), and the fault is late in earthquake cycle with a locking depth reaching to ~15 km (Ambraseys and Bilham, 2003; Szeliga et al., 2009), causing surface velocities to be slower than might be the case if the mid-crust hadn't flowed so much early in the earthquake cycle. 2) Much of the deformation within this area in the past was taken up on the Chaman fault. However, changing fault properties (such as frictional strength) of this fault and the other candidate structures that may take up the plate motion may have changed relative to one another, which may favor current motions along other structures rather than the Chaman fault. In this scenario, the GPS data are reflective of the current Chaman fault loading rate, but plate-boundary motions are simply being accommodated elsewhere due to changing fault properties.

The displacement along the Chaman fault measured during this study represents many earthquake cycles spanning the last ~35 kyr. These earthquakes may account for the overall average displacement and thus restricting the impact of inter- and/or post-seismic relaxations, which has a major impact on the GPS and InSAR constrained slip-rates (e.g. Meade, 2007). Seismic activity including instrumental data from 1974 until 2010 as well as the two historic earthquakes (Mw ~ 6.7 1892 Chaman earthquake and Mw ~ 7.7 1935 Quetta earthquake) (Fig. 8), as summarized by Ambraseys and Bilham (2003), shows fewer events than the expected as compared to the total convergence accommodated by the boundary zone (Molnar and Dayem, 2010). Most of the activity is predicted within the central part of the Chaman fault system with a slip-rate of 49.1 mm/yr within a zone of 60 km, which includes the Chaman fault and our study area (Fig. 8). While in north and south of this zone the slip-rate is estimated to be 3.1 mm/yr and 0.5 mm/yr, respectively. Based on the seismic record of the last century Ambraseys and Bilham (2003) predicted a slip deficit that could be enough to trigger one or more events of $M_w > 7$ in this 60 km wide western plate boundary zone. They also concluded that the seismic activity of the past century in the region is not representative of the long-term slip-rate within the plate boundary zone. This further implies that the fault segment which is the center of most of the studies (the northern part of the Chaman fault that runs in Pakistan) is moving slow at this stage in its poorly understood seismic cycle (Szeliga et al., 2012) as compared to the cumulative geomorphic slip-rate as has been noticed along other faults such as the San Andreas fault system in Southern California (Chuang and Johnson, 2011). However, the
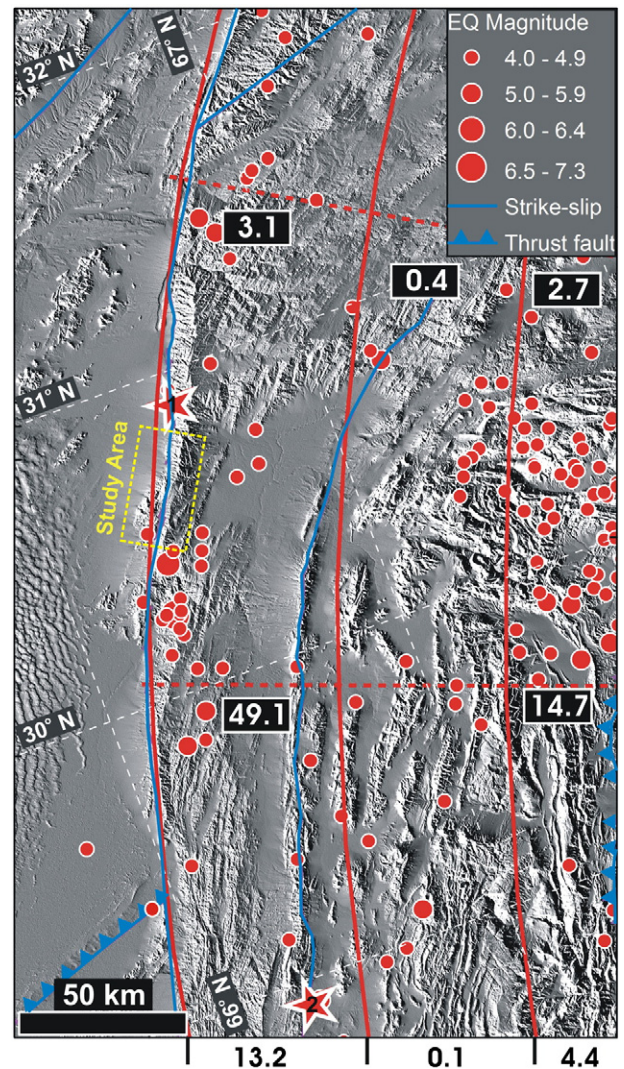
Fig. 8. Seismicity within a part of the western Indian plate boundary zone including instrumental earthquake data from 1974 to 2010 with events larger than Mw 4.0 (from USGS earthquake catalog) and the historical Mw ~ 6.7 Chaman earthquake of 1892 (star 1) and Mw ~ 7.7 Quetta earthquake of 1935 (star 2) (Ambraseys and Bilham, 2009). Seismic activity is concentrated east of the Chaman fault with almost no seismicity in the west of the fault. The three 60 km wide zones (red north–south lines) were estimated by Ambraseys and Bilham (2003) based on about 200 years earthquake data showing an average slip-rate of 49.1 mm/yr in the western zone with a cumulative moment release equivalent to ~13.2 mm/yr slip-rate. This zone includes the Chaman fault which limits the boundary zone in the west. Numbers in black rectangles in each 60 km swath is the equivalent slip-rate of the moment release, while black numbers at the bottom of the figure resemble slip-rate equivalent to the reduction in moment release. Active to recently active strike–slip and thrust faults are modified after Ruleman et al., 2007.

earthquake cycle for the Chaman fault system is poorly defined across many time intervals and, of course, a more comprehensive dataset needs to be obtained from future studies. Moreover, plate boundary velocities estimated from InSAR data spanning a year and a half show episodic slip along a creeping Chaman fault associated with a $M_w5.0$ earthquake (Furuya and Satyabala, 2008), implying larger displacements with surface ruptures associated with high magnitude events such as the 1892 Chaman earthquake, which are prevalent in this region (Lawrence et al., 1992). InSAR investigations on longer timescales may be able to resolve the strain distribution within the plate boundary zone.

Fault inversion within the shear zone may account for the presently slower displacements (18 ± 1 mm/yr) along the Chaman fault, which

is a common characteristic of strain distribution within the plate boundary (Bennett et al., 2004). The Ghazaband, Gardez and Ornach–Nal faults (Fig. 1), which mark the eastern limit of the shear zone (Lawrence et al., 1992), might be the candidates for strain trade-off between the Chaman fault and these other faults. However, it is very unlikely that strain trade-off can occur on a shorter timescale ($<10^6$ yr) and as such these complimentary faults within the shear zone are responsible for sparse tectonic activity in Quaternary (Lawrence et al., 1992). Another possibility which may be causing the disparity might be the convergence of the fold thrust belts along this transpressive plate boundary resulting in strain partitioning rates ranging from 3 to 6 mm/yr (Bernard et al., 2000; Szeliga et al., 2009) to 13 ± 3 mm/yr (Ambraseys and Bilham, 2003) (Fig. 8). Strain partitioning is essential to the geometry of the azimuth of the Indian Plate motion relative to Eurasia (N12°E) and strike of the Chaman fault (N34°E) (Molnar and Dayem, 2010), which implies strain distribution within the northwestern rigid Indian Plate boundary, although most of the strain is accommodated along the Chaman fault.

5. Conclusions

We obtained a slip-rate of 33.3 ± 3.0 mm/yr along a strand of the Chaman fault; this is the first geomorphic based rate derived from an actual displacement along this structure. Strain partitioning within the plate boundary zone may be the main factor causing the disparity in geodetic and geomorphic slip-rates along the Chaman fault; however, transient strain accumulation within in the plate boundary zone is a possible explanation for a faster slipping Chaman fault with a low viscosity mid-crust under the Chaman fault system, measured on a 35 ka time-scale, which may be moving slow at its present stage in the seismic cycle. Interpretations of current geodetic and geomorphic datasets conclude that strike–slip faults in the Chaman transform zone along the Indian plate boundary have a complex history and evolution.

Supplementary data to this article can be found online at http://dx.doi.org/10.1016/j.tecto.2013.09.009.

References

Ambraseys, N., Bilham, R., 2003. Earthquakes and associated deformation in northern Baluchistan. Bull. Seismol. Soc. Am. 93, 1573–1605.

Ambraseys, N., Bilham, R., 2009. The tectonic setting of Bamiyan and the seismicity in and near Afghanistan for the past 12 centuries. The Destruction of the Giant Buddha Statues in Bamiyan, chapt.7. UNESCO Pub., Paris, pp. 67–94.

Avouac, J.-P., Tapponnier, P., 1993. Kinematic model of active deformation in Asia. Geophys. Res. Lett. 20, 895–898.

Azor, A., Keller, E.A., Yeats, R.S., 2002. Geomorphic indicators of active fold growth: South Mountain–Oak Ridge anticline, Ventura basin, southern California. GSA Bull. 114, 745–753.

Balco, G., Stone, J.O., Lifton, N.A., Dunai, T.J., 2008. A complete and easily accessible means of calculating surface exposure ages or erosion rates from ^{10}Be and ^{26}Al measurements. Quat. Geochronol. 3, 174–195.

Bendick, R., Bilham, R., Freymueller, J., Larson, K., Yin, G., 2000. Geodetic evidence for a low slip rate in the AltynTagh fault system. Nature 404, 69–72.

Bennett, R.A., Friedrich, A.M., Furlong, K.P., 2004. Codependent histories of the San Andreas and San Jacinto fault zones from inversion of fault displacement rates. Geology 32, 961–964.

Bernard, M., Shen-Tu, B., Holt, W., Davis, D., 2000. Kinematics of active deformation in the Sulaiman Lobe and Range, Pakistan. J. Geophys. Res. 105. http://dx.doi.org/10.1029/1999JB900405.

Beun, N., Border, P., Carbonnel, J., 1979. Premières données quantitative relatives' au coulissage du décrochement de Chaman (Afghanistan du sud-est). C. R. Acad. Sci. Paris 288, 931–934.

Blisniuk, K., Rockwell, T., Owen, L.A., Oskin, M., Lippincott, C., Caffee, M.W., Dortch, J., 2010. Late Quaternary slip rates gradient defined using high-resolution topography and ^{10}Be dating of offset landforms on the southern San Jacinto Fault zone, California. J. Geophys. Res. 115. http://dx.doi.org/10.1029/2009JB006346.

Burbank, D., Meigs, A., Brozovic, N., 1996. Interactions of growing folds and coeval depositional systems. Basin Res. 8, 199–223.

Carter, A., Najman, Y., Bahroudi, A., Bown, P., Garzanti, E., Lawrence, R.D., 2010. Locating earliest records of orogenesis in western Himalaya: evidence from Paleogene sediments in the Iranian Makran region and Pakistan Katawaz basin. Geology 38, 807–810.

Chen, Z., Burchfiel, B.C., Liu, Y., King, R.W., Royden, L.H., Tang, W., Wang, E., Zhao, J., Zhang, X., 2000. Global positioning system measurements from eastern Tibet and their implications for India/Eurasia intercontinental deformation. J. Geophys. Res. 105, 16215–16227.

Chevalier, M.L., Ryerson, F.J., Tapponnier, P., Finkel, R.C., der Woerd, J.V., Haibing, L., Qing, L., 2005. Slip-rate measurements on the Karakorum Fault may imply secular variations in fault motion. Science 307, 411–414.

Chuang, R.Y., Johnson, K.M., 2011. Reconciling geologic and geodetic model fault slip-rate discrepancies in Southern California: consideration of non-steady mantle flow and lower crustal fault creep. Geology 39, 627–630.

Cowgill, E., Gold, R.D., Chen, X.H., Wang, X.F., Arrowsmith, J.R., Southon, J., 2009. Low Quaternary slip rate reconciles geodetic and geologic rates along the Altyn Tagh fault, northwestern Tibet. Geology 37, 647–650.

England, P., Houseman, G., 1986. Finite strain calculations of continental deformation: 2. Comparison with the India–Asia collision zone. J. Geophys. Res. 91, 3664–3676.

England, P., Molnar, P., 2005. Late Quaternary to decadal velocity fields in Asia. J. Geophys. Res. 110. http://dx.doi.org/10.1029/2004JB003541.

Frankel, K.L., Owen, L.A., 2013. Transform plate margins and strike-slip fault systems. In: Shroder J. (Editor in Chief), Owen, L.A. (Ed.), Treatise on Geomorphology. Tectonic Geomorphology, vol. 5. Academic Press, San Diego, CA, pp. 37–70.

Frankel, K.L., Brantley, K.S., Dolan, J.F., Finkel, R.C., Klinger, R.E., Knott, J.R., Machette, M.N., Owen, L.A., Phillips, F.M., Slate, J.L., Wenicke, B.P., 2007a. Cosmogenic ^{10}Be and ^{36}Cl geochronology of offset alluvial fans along the northern Death Valley fault zone: implications for transient strain in the eastern California shear zone. J. Geophys. Res. 112, B06407. http://dx.doi.org/10.1029/2006JB004350.

Frankel, K.L., Dolan, J.F., Finkel, R.C., Owen, L.A., Hoeft, J.S., 2007b. Spatial variations in slip rate along the Death Valley-Fish Lake Valley fault system determined from LiDAR topographic data and cosmogenic ^{10}Be geochronology. Geophys. Res. Lett. 34, LI8303. http://dx.doi.org/10.1029/2007GL030549.

Frankel, K.L., Dolan, J.F., Owen, L.A., Ganev, P., Finkel, R.C., 2011. Spatial and temporal constancy of seismic strain release along an evolving segment of the Pacific-North America plate boundary. Earth Planet. Sci. Lett. 304, 565–576.

Furuya, M., Satyabala, S.P., 2008. Slow earthquake in Afghanistan detected by InSAR. Geophys. Res. Lett. 35. http://dx.doi.org/10.1029/2007GL033049.

He, J., Chéry, J., 2008. Slip rates of the Altyn Tagh, Kunlun and Karakorum faults (Tibet) from 3D mechanical modeling. Earth Planet. Sci. Lett. 274, 50–58.

Heisinger, B., Lal, D., Jull, A.J.T., Kubik, P., Ivy-Ochs, S., Knie, K., Nolte, E., 2002. Production of selected cosmogenic radionuclides by muons: 2. Capture of negative muons. Earth Planet. Sci. Lett. 200, 357–369.

Hoeft, J.S., Frankel, K.L., 2010. Temporal variations in extension rate on the Lone Mountain fault and strain distribution in the eastern California shear zone–Walker Lane. Geosphere 6, 917–936.

Jadoon, I.A.K., Khurshid, A., 1996. Gravity and tectonic model across the Sulaiman fold belt and the Chaman fault zone in western Pakistan and eastern Afghanistan. Tectonophysics 254, 89–109.

Keller, E.A., DeVecchio, D.E., 2013. Tectonic geomorphology of active folding and development of transvers drainage. In: Owen, L.A. (Ed.), Tectonic Geomorphology. Treatise on Geomorphology, 5. Academic Press, San Diego, pp. 129–147.

Klootwijk, C.T., Gee, J.S., Peirce, J.W., Smith, G.M., McFadden, P.L., 1998. An early India–Asia contact: paleomagnetic constraints from Ninety East Ridge, ODP Leg 121. Geology 20, 395–398.

Kubik, P.W., Ivy-Ochs, S., 2004. A re-evaluation of the 0–10 ka ^{10}Be production rate for exposure dating obtained from the Köfels (Austria) landslide. Nuclear Instruments and Methods B 223–224, 618–622.

Lal, D., 1991. Cosmic ray labeling of erosion surfaces: in situ nuclide production rates and erosion models. Earth Planet. Sci. Lett. 104, 424–439.

Lawrence, R.D., Yeats, R.S., 1979. Geological reconnaissance of the Chaman fault in Pakistan. In: Farah, A., DeJong, K.A. (Eds.), Geodynamics of Pakistan, pp. 351–357.

Lawrence, R.D., Yeats, R.S., Khan, S.H., Subhani, A.M., Bonelli, D., 1981. Crystalline rocks of the Spinatizha area, Pakistan. J. Struct. Geol. 3, 449–457.

Lawrence, R.D., Nakata, S.H., Khan, T., 1992. Chaman fault, Pakistan–Afghanistan. Ann. Tectonicae 6, 196–223.

Meade, B.J., 2007. Present-day kinematics at the India–Asia collision zone. Geology 35 (1), 81–84.

Mériaux, A.-S., Ryerson, F.J., Tapponnier, P., Van der Woerd, J., Finkel, R.C., Xu, X., Xu, Z., Caffee, M.W., 2004. Rapid slip along the central AltynTagh Fault: morphochronologic evidence from Cherchen He and SulamuTagh. J. Geophys. Res. 109. http://dx.doi.org/10.1029/2003JB002558.

Mériaux, A.-S., Tapponnier, P., Ryerson, F.J., Xiwei, X., King, G., Van der Woerd, J., Finkel, R.C., Haibing, L., Caffee, M.W., Zhiqin, X., Wenbin, C., 2005. The Aksay segment of the northern AltynTagh Fault: tectonic geomorphology, landscape evolution, and Holocene slip rate. J. Geophys. Res. 110. http://dx.doi.org/10.1029/2004JB003210.

Mohadjer, S., Bendick, R., Ischuk, A., Kuzikov, S., Kostuk, A., Saydullaev, U., Lodi, S., Kakar, D.M., Wasy, A., Khan, M.A., Molnar, P., Bilham, R., Zubovich, A.V., 2010. Partitioning of India–Eurasia convergence in the Pamir-Hindu Kush from GPS measurements. Geophys. Res. Lett. 37. http://dx.doi.org/10.1029/2009GL041737.

Molnar, P., Dayem, K., 2010. Major intracontinental strike–slip faults and contrasts in lithospheric strength. Geosphere 6, 444–467.

Molnar, P., Stock, J.M., 2009. Slowing of India's convergence with Eurasia since 20 Ma and its implications for Tibetan mantle dynamics. Tectonics 28. http://dx.doi.org/10.1029/2008TC002271.

Molnar, P., Tapponnier, P., 1975. Cenozoic tectonics of Asia: effects of a continental collision. Science 189, 419–426.

Nishiizumi, K., Winterer, E., Kohl, C., Klein, J., Middleton, R., Lal, D., Arnold, J., 1989. Cosmic ray production rates of ^{26}Al and ^{10}Be in quartz from glacially polished rocks. J. Geophys. Res. 94, 17907–17915.

Nishiizumi, K., Imamura, M., Caffee, M., Southon, J., Finkel, R., McAnich, J., 2007. Absolute calibration of Be-10 AMS standards. Nucl. Inst. Methods Phys. Res. B 258, 403–413.

Oskin, M., Perg, L., Blumentritt, D., Mukhopadhyay, S., 2007. Slip rate of the Calico fault: implications for geologic versus geodetic rate discrepancy in the Eastern California Shear Zone. J. Geophys. Res. 112. http://dx.doi.org/10.1029/2006JB004451.

Owen, L.A., Caffee, M.W., Bovard, K.R., Finkel, R.C., Sharma, M.C., 2006. Terrestrial cosmogenic nuclide surface exposure dating of the oldest glacial successions in the Himalayan orogen: Ladakh Range, northern India. GSA Bull. 118, 383–392. http://dx.doi.org/10.1130/B25750.1.

Owen, L.A., Frankel, K.L., Knott, J.R., Reynhout, S., Finkel, R.C., Dolan, J.F., Lee, J., 2011. Beryllium-10 terrestrial cosmogenic nuclide surface exposure dating of Quaternary landforms in Death Valley. Geomorphology 125, 541–557.

Pearce, S.A., Pazzaglia, F.J., Eppes, M.C., 2004. Ephemeral stream response to growing folds. Geol. Soc. Am. Bull. 116, 1223–1239.

Peltzer, G., Saucier, F., 1996. Present-day kinematics of Asia derived from geologic fault rates. J. Geophys. Res. 101, 27943–27956.

Peltzer, G., Tapponnier, P., 1988. Formation and evolution of strike–slip faults, rifts, and basins, during the India–Asia collision: an experimental approach. J. Geophys. Res. 93, 15085–15117. http://dx.doi.org/10.1029/JB093iB12p15085.

Phillips, R.J., Parrish, R.R., Searle, M.P., 2004. Age constraints on ductile deformation and long-term slip rates along the Karakoram fault zone, Ladakh. Earth Planet. Sci. Lett. 226, 305–319.

Qayyum, M., Niem, A.R., Lawrence, R.D., 1996. Newly discovered Paleogene deltaic sequence in Katawaz basin, Pakistan, and its tectonic implications. Geology 24, 835–838.

Ruleman, C.A., Crone, A.J., Machette, M.N., Haller, K.M., Rukstales, K.S., 2007. Map and database of probable and possible Quaternary faults in Afghanistan. U.S. Geological Survey Open-File Report 2007-1103. (39 pp.).

Shen, Z., Wang, M., Li, Y., Jackson, D.D., Yin, A., Dong, D., Fang, P., 2001. Crustal deformation along the AltynTagh fault system, western China, from GPS. J. Geophys. Res. 106, 30607–30622.

Stone, J.O., 2000. Air pressure and cosmogenic isotope production. J. Geophys. Res. 105, 23753–23759.

Szeliga, W., Bilham, R., Schelling, D., Kakar, D.M., Lodi, S., 2009. Fold and thrust partitioning in a contracting fold belt: insights from the 1931 Mach earthquake in Baluchistan. Tectonics 28. http://dx.doi.org/10.1029/2008TC002265.

Szeliga, W., Bilham, R., Kakar, D.M., Lodi, S., 2012. Interseismic strain accumulation along the western boundary of the Indian subcontinent. J. Geophys. Res. 117, B08404. http://dx.doi.org/10.1029/2011JB008822.

Tapponnier, P., Xu, Z., Roger, F., Meyer, B., Arnaud, N., Wittlinger, G., Yang, J., 2001. Oblique stepwise rise and growth of the Tibet Plateau. Science 294, 1671–1677.

Taylor, M., Yin, A., 2009. Active structures of the Himalayan–Tibetan orogen and their relationships to earthquake distribution, contemporary strain field, and Cenozoic volcanism. Geosphere 5, 199–214.

Thatcher, W., 2007. Micro-plate model for the present-day deformation of Tibet. J. Geophys. Res. 112. http://dx.doi.org/10.1029/2005JB004244.

Ul-Hadi, S., Khan, S.D., Owen, L.A., Khan, A.S., 2012. Geomorphic response to an active transpressive regime: a case study along the Chaman strike–slip fault, Western Pakistan. Earth Surf. Process. Landforms 38, 25–264.

Van der Woerd, J., Ryerson, F.J., Tapponnier, P., Gaudemer, Y., Finkel, R., Meriaux, A.S., Caffee, M.W., Guoguang, Z., Qunlu, H., 1998. Holocene left-slip rate determined by cosmogenic surface dating on the Xidatan segment of the Kunlun fault (Qinghai, China). Geology 26, 695–698.

Van der Woerd, J., Ryerson, F.J., Tapponnier, P., Meriaux, A.S., Gaudemer, Y., Meyer, B., Finkel, R., Caffee, M.W., Guoguang, Z., Zhiqin, X., 2000. Uniform slip-rate along the Kunlun Fault: implications for seismic behavior and large-scale tectonics. Geophys. Res. Lett. 27, 2353–2356.

Wheeler, R.L., Bufe, C.G., Johnson, M.L., Dart, R.L., 2005. Seismotectonic map of Afghanistan with annotated bibliography. U.S. Geological Survey Open-File Report 2005-1264. (31 pp.).

Wright, T.J., Parsons, B., England, P.C., Fielding, E.J., 2004. InSAR observations of low slip rates on the major faults of western Tibet. Science 305, 236–239.

Yin, A., Harrison, T.M., 2000. Geologic evolution of the Himalayan–Tibetan orogen. Ann. Rev. Earth Planet. Sci. 28, 211–280.

Zhang, P.Z., Molnar, P., Xu, X., 2007. Late Quaternary and present-day rates of slip along the Altyn Tagh Fault, northern margin of the Tibetan Plateau. Tectonics 26. http://dx.doi.org/10.1029/2006TC002014.

Zubovich, A.V., Wang, X.-Q., Scherba, Y.G., Schelochkov, G.G., Reilinger, R., Reigber, C., Mosienko, O.I., Molnar, P., Michajljow, W., Makarov, V.I., Li, J., Kuzikov, S.I., Herring, T.A., Hamburger, M.W., Hager, B.H., Dang, Y., Bragin, V.D., Beisenbaev, R.T., 2010. GPS velocity field for the Tien Shan and surrounding regions. Tectonics 29 (TC6014), 1–23. http://dx.doi.org/10.1029/2010TC002772.